Dalton Transactions

ROYAL SOCIETY OF CHEMISTRY

PAPER

View Article Online
View Journal | View Issue

Cite this: *Dalton Trans.*, 2025, **54**, 10358

A salophen-type macrocyclic Schiff base ligand and its metal complexes: exploring *in vitro* anticancer efficacy *via in silico* topoisomerase IIβ enzyme targeting†

Monika Yadav,[a] Deepak Yadav,[b] Dharam Pal Singh[a] and Jitander Kumar Kapoor *[a]

Cancer persists as a principal cause of global mortality. Despite significant progress in cancer therapeutics in recent decades, chemotherapy remains a primary modality for cancer treatment. Based on their mechanism of action, commonly used chemotherapeutic agents can be classified into several categories, including topoisomerase inhibitors. Here, a newly synthesized salophen-type macrocyclic Schiff-base ligand (5*E*,19*E*)-3-bromo-12,13-dihydrodibenzo[*e*,*m*]pyrido[2,3-*i*][1,4]dioxa[8,11]diazacyclotetradecine (**4**) and its metal complexes (**5a–5d**) have been reported as potent anticancer agents exhibiting topoisomerase IIβ inhibitory activity. *In silico* docking studies elucidated their binding interactions with the active site of the topoisomerase IIβ enzyme (PDB ID: 4G0V). The docking simulation results indicated that the ligand exhibited its most favorable interaction with a binding energy of −10.3 kcal mol^{-1}. Also, *in vitro* anticancer studies using the MTT assay against the HepG2 liver cancer cell line corroborated these findings, demonstrating that the ligand exhibited its strongest inhibitory action with an IC_{50} of 0.09 μM, comparable to that of the standard anticancer drug doxorubicin.

Received 28th April 2025,
Accepted 1st June 2025

DOI: 10.1039/d5dt00993f

rsc.li/dalton

1. Introduction

Cancer is a condition where cells grow out of control, leading to the development of a solid mass, or tumor, in the affected area of the body and which might metastasize to other parts of the body through circulatory and lymphatic systems. Using oxygen and other nutrients from the body, cancer cells expand by interfering with the growth of healthy cells.[1] Hence, cancer is an aberrant cell state in which the cells proliferate in an uncontrolled manner and develop deadly tumors, which causes deaths of millions of people annually. In 2018, the World Health Organization ranked cancer as the 2nd most common cause of death worldwide among this group of diseases. The Global Cancer Observatory estimated that there were 19.9 million new instances of cancer worldwide in 2022, with 9.7 million cancer-related deaths [https://gco.iarc.who.int/today/en].

Currently available cancer treatments are surgery, chemotherapy, immunotherapy, and radiotherapy. In chemotherapy, low molecular weight drugs are specifically used to destroy the tumor cells or at least inhibit their proliferation. However, there are side effects of many cytotoxic agents including gastrointestinal tract lesions, hair loss, bone marrow suppression, nausea, and the development of clinical resistance. These side effects are due to the action of cytotoxic agents against both the tumor cells and healthy cells of the body.[2]

Despite the growing popularity of targeted treatments and immunotherapies, chemotherapeutic medications, biologics, and immune-mediated therapies continue to play crucial roles in cancer research and clinical practice. Nevertheless, weak patient response is frequently the result of developing resistance to traditional treatment. The development of innovative, effective, and non-toxic medications for the treatment of cancer is urgently needed, especially in view of the high toxicity of many current chemotherapeutic treatments. Chemotherapy drugs may be divided into a number of classes based on a number of factors, including their chemical framework and function. Depending on the mode of action, these can be classified as topoisomerase inhibitors, antimetabolites, alkylating agents, mitotic spindle inhibitors, and others.[3,4]

Alkylating agents have a number of drawbacks such as higher toxicity and lower selectivity, while reagents that target

[a]*Department of Chemistry, National Institute of Technology Kurukshetra-136119, Haryana, India. E-mail: jkkapoor@nitkkr.ac.in*
[b]*Department of Experimental Medicine and Biotechnology, PGIMER, Chandigarh-160012, India*

† Electronic supplementary information (ESI) available. See DOI: https://doi.org/10.1039/d5dt00993f

topoisomerases are more selective.[5] DNA topoisomerases are essential enzymes that meticulously regulate the supercoiling of DNA, a critical aspect of its 3-D structure. This precise control over DNA topology is fundamental for the survival of all living organisms. By transiently breaking and rejoining DNA strands, topoisomerases alleviate torsional stress, enabling vital cellular processes such as DNA replication, transcription, chromosome segregation, and recombination to proceed efficiently and accurately.[5,6]

Topoisomerase inhibitors disrupt DNA replication by targeting topoisomerase enzymes, leading to DNA damage. Specifically, topoisomerase I inhibitors (*e.g.*, irinotecan and topotecan) interfere with the re-ligation step of topoisomerase I, resulting in single-stranded DNA breakages while topoisomerase II inhibitors [e.g., etoposide, teniposide, and anthracyclines such as idarubicin, daunorubicin, and doxorubicin (DOX)] interfere with the re-ligation step of topoisomerase II, leading to double-stranded DNA breakages.[7]

For the invention of new anticancer drugs, designing drugs to inhibit or target the topoisomerase II enzyme is a promising strategy. As topoisomerase II plays a crucial role in DNA replication and cell division, processes that are often dysregulated in cancer cells, inhibiting this enzyme can effectively disrupt cancer cell proliferation. This strategy aligns well with the growing trend of targeted drug delivery methods, as researchers explore ways to deliver topoisomerase II inhibitors specifically to tumor cells, further enhancing their effectiveness and reducing off-target effects.[8]

The Schiff-base moiety (–HC═N–) represents a significant and versatile structural motif in medicinal chemistry, demonstrating promising activity and functioning as an anti-bacterial, anti-inflammatory, antiviral, anti-fungal, and anticancer agent.[9–15] Transition metal complexes incorporating Schiff-base ligands have garnered considerable interest due to their broad spectrum of biological and pharmaceutical properties. Also, the inherent tunability of Schiff-base and macrocyclic scaffolds allows for structural modifications that can enhance their selectivity for cancer cells and their ability to be incorporated into target drug-delivery systems.[16] By conjugating these ligands or their metal complexes to nanoparticles, antibodies, or other targeting moieties, researchers aim to achieve precise delivery to tumor sites, maximizing their interaction with topoisomerase II in cancer cells while minimizing systemic exposure and toxicity.[17]

A significant advantage of the Schiff-base reaction lies in its capacity to generate "multi-azomethine functionalized compounds" from polycarbonyl and/or polyamine precursors. Within this class, salen and salophen-type bis-Schiff bases have been extensively investigated,[18–26] with a substantial body of the literature and reviews highlighting their intriguing physicochemical properties and diverse potential applications, as well as those of their metal complexes.[27–32] Salen and salophen ligands are synthesized through the condensation of one equivalent of aliphatic/aromatic diamines and two equivalents of salicylaldehyde derivatives. The nuclearity of salophen and salen metal complexes can indeed be increased through the utilization of macrocyclic or bi-compartmental N_2O_2–O_2X_2 salen and salophen derivatives. These specialized ligands feature additional atoms or groups (X = N, O, or S) strategically positioned at the *meta*-position on their salicylic aromatic rings.[33–36]

In recent years, many studies have been reported which show salophen metal complexes as promising anticancer agents.[10,37–39]Also, Yilmaz *et al.* (2023) reported Schiff bases as direct topoisomerase inhibitors.[40] Topkaya *et al.* (2022) demonstrated that salen Schiff-base complexes exhibit inhibitory activity against both topoisomerase I and II.[41] Many such studies are available in the literature and show that Schiff-base ligands and their metal complexes act as inhibitors of topoisomerase, which is a crucial target in cancer treatment. Our research group has also been working in this field for the last two years. In our recent reports, we have shown that macrocyclic Schiff bases and their metal complexes are topoisomerase IIβ inhibitors.[42,43]

Our focus has primarily been on the design, synthesis, and evaluation of macrocyclic Schiff bases and their metal complexes. This growing body of evidence strongly supports the exploration of Schiff-base ligands and their metal complexes, particularly macrocyclic derivatives, as a promising avenue for the generation of new anticancer therapeutics targeting the topoisomerase IIβ enzyme.

Having thoroughly reviewed the existing literature, including studies highlighting the anticancer potential of salophen metal complexes and topoisomerase inhibitory activity of various Schiff-base derivatives, we were motivated to design and synthesize a novel salophen-type macrocyclic Schiff-base ligand and its corresponding metal complexes.

Herein, we report the synthesis and characterization of a novel salophen-type macrocyclic Schiff-base ligand (**4**) and its transition metal complexes (**5a–5d**). The new compounds were characterized using various spectroscopic techniques, including FT-IR, UV-Vis, NMR, HRMS, and ESR, and thermal analysis *via* TGA. Furthermore, the potential of these newly synthesized compounds as topoisomerase IIβ inhibitors was investigated through molecular docking studies employing AutoDock Vina and GOLD software. Their anticancer activity was evaluated against the HepG2 cell line using the MTT assay. Additionally, hemolytic studies were conducted to assess their toxicity profile against normal hRBCs.

2. Results and discussion

The new salophen-type Schiff-base ligand and its complexes were synthesized *via* a multiple-step reaction, as shown in Scheme 1, and further purified by column chromatography. The formation of the synthesized compounds was confirmed by various spectroscopic techniques. All the compounds are stable at room temperature and soluble in DMSO and DMF only.

2.1. IR analysis

Infrared (IR) spectroscopy provided definitive evidence for the successful synthesis of the macrocyclic ligand and its corres-

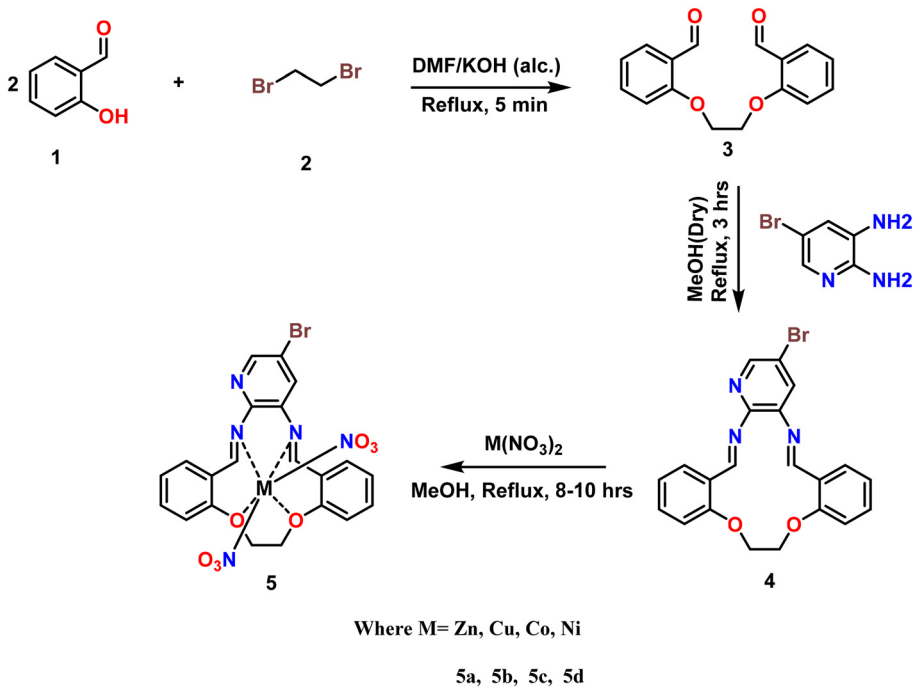

Scheme 1 Schematic representation of the synthesis of the macrocyclic Schiff-base ligand and its complexes.

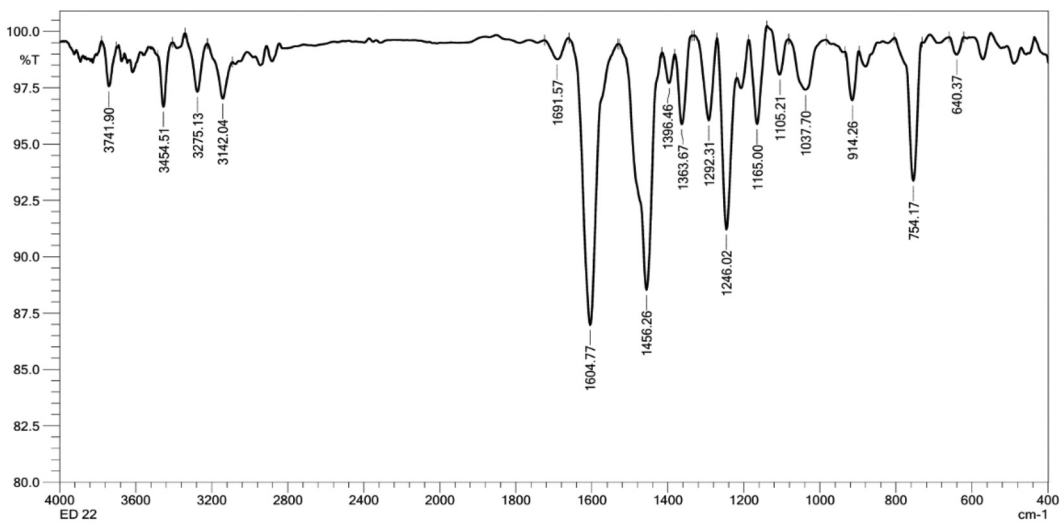

Fig. 1 IR spectrum of ligand **4**.

ponding metal complexes. The formation of the Schiff-base ligand was confirmed by the characteristic stretching vibration of the imine bond (ν(C═N)) observed at 1604 cm^{-1} (Fig. 1).[44] This observation, coupled with the absence of bands corresponding to the primary amine (ν_{as} (NH_2) at 3250 cm^{-1} and ν_s (NH_2) at 3380 cm^{-1}) and the carbonyl group of bis-aldehyde (ν(C═O) at 1685 cm^{-1}), unequivocally supports the occurrence of a condensation reaction.

In the metal complexes, the ν(C═N) stretching vibration exhibited a shift to lower wavenumbers (1600–1604 cm^{-1}, Fig. S4–S7†) compared to the free ligand, indicating coordination of the imine nitrogen to the metal ions. The presence of aromatic C–H stretching vibrations, observed at around 3057 cm^{-1}, was consistent across both the ligand and complexes. Crucially, new bands in the regions of 595–597 cm^{-1} and 450–460 cm^{-1} emerged in the complex spectra, which are assigned to the M–N and M–O stretching vibrations.[41] These bands directly confirm the coordination of the metal ion through the nitrogen and oxygen atom of azomethine and ether, respectively. Also, the appearance of new bands in the

infrared spectrum of the complex at around 1452 (asymmetric stretching), 1242 (symmetric stretching), 1045 (out of plane bending), 830, and 752 cm^{-1} (in plane bending) provides evidence consistent with the coordination of the nitrate (NO_3^-) group as the monodentate ligand with the M–O bond. The specific positions and splitting patterns of these bands can be indicative of the coordination mode.[45–47]

In summary, the IR spectral data collectively demonstrate the successful formation of the macrocyclic Schiff-base ligand and its subsequent coordination to metal ions, providing strong evidence for the desired complexation.

2.2. NMR analysis

The structural characterization of the synthesized macrocyclic ligand was achieved using ^1H and ^{13}C nuclear magnetic resonance (NMR) spectroscopy, performed in DMSO-d_6. The ^1H-NMR spectrum exhibited a characteristic singlet at δ 8.76 ppm, assigned to the imine protons (HC═N), confirming the condensation reaction[45,46,48] (Fig. 2). A singlet resonance at δ 4.60 ppm was attributed to the methylene protons (–OCH_2–). The pyridine ring protons displayed doublet signals at δ 7.19 and δ 7.02 ppm, consistent with an aromatic system. The aromatic protons of the salicylaldehyde moieties were observed as a complex multiplet within the region of δ 7.51–8.15 ppm. Notably, the absence of the aldehydic proton signal at δ 10.3 ppm, coupled with the presence of the imine proton signal at δ 8.76 ppm, definitively confirmed the formation of the Schiff-base ligand.

The ^{13}C-NMR spectrum further corroborated the structural assignment. A distinct signal at δ 158.77 ppm was observed, corresponding to the imine carbon (C═N), as shown in Fig. 3.[49] Additionally, a signal at δ 68.0 ppm was assigned to the –OCH_2– carbon.[50] These signals, in conjunction with the ^1H-NMR data, provided compelling evidence for the successful synthesis of the desired macrocyclic ligand.

2.3. Mass spectral analysis

High-resolution mass spectrometry (HRMS) was utilized to confirm the molecular compositions of the synthesized Schiff-base complexes. This technique provides accurate mass-to-charge (m/z) ratios, serving as a powerful tool in coordination chemistry for verifying the presence and integrity of the expected molecular ions. It is also used to determine the structural properties of the investigated species and to ascertain whether the complexes are monomeric or polymeric.[43] The experimental m/z values obtained from HRMS (Fig. S8–S12†) revealed excellent agreement with the calculated values, validating the proposed structures of the ligand and its complexes **5a–5d**. Specifically, the molecular ion peaks [M + H] were observed at m/z values of 422.0506 (calculated: 422.2820) for **4**, 609.0070 (calculated: 608.9474) for **5a**, 606.993 (calculated: 607.9478) for **5b**, 607.058 (calculated: 607.940) for **5c**, and 607.0620 (calculated: 602.9500) for **5d**.

2.4. Electronic spectral analysis

The electronic absorption spectra of the synthesized complexes were recorded in 1×10^{-5} M DMSO solution at room temperature to elucidate their geometries (Fig. 4). The spectrum of the Zn(II) complex (**5a**) exhibited absorption bands at 324 nm and 388 nm, assigned to $\pi \rightarrow \pi^*$ and $n \rightarrow \pi^*$ transitions, respectively. These transitions are characteristic of the absorption of the aromatic ring and imine chromophore, consistent with expectations for Zn(II) octahedral complexes.

The Co(II) complex (**5c**) displayed a distinct absorption band at 326 nm with a shoulder at 356 nm, also attributed to $\pi \rightarrow \pi^*$ and $n \rightarrow \pi^*$ transitions. Also, there is a band near

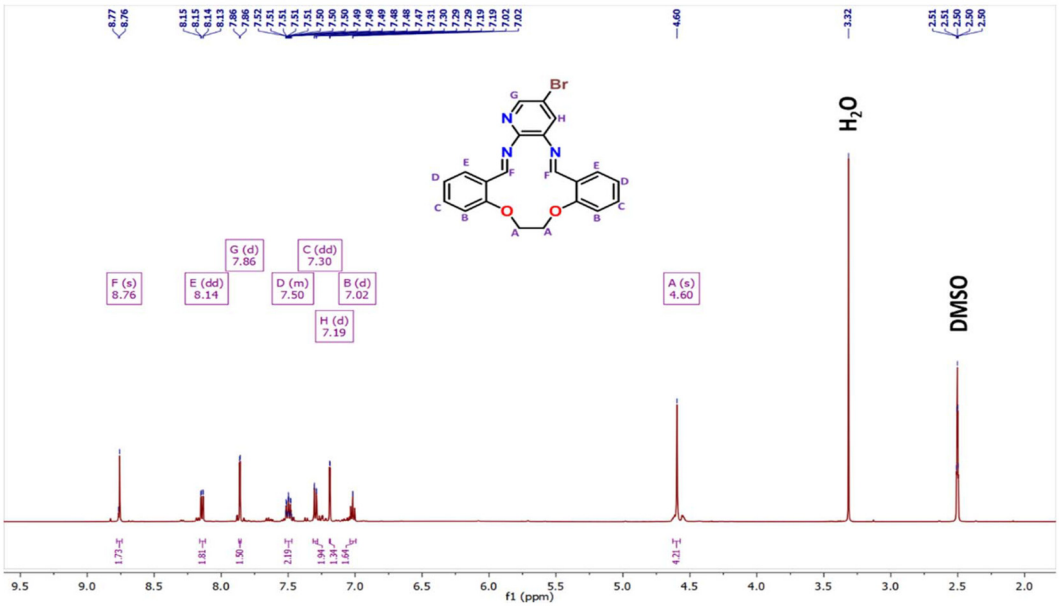

Fig. 2 ^1H-NMR spectrum of ligand **4**.

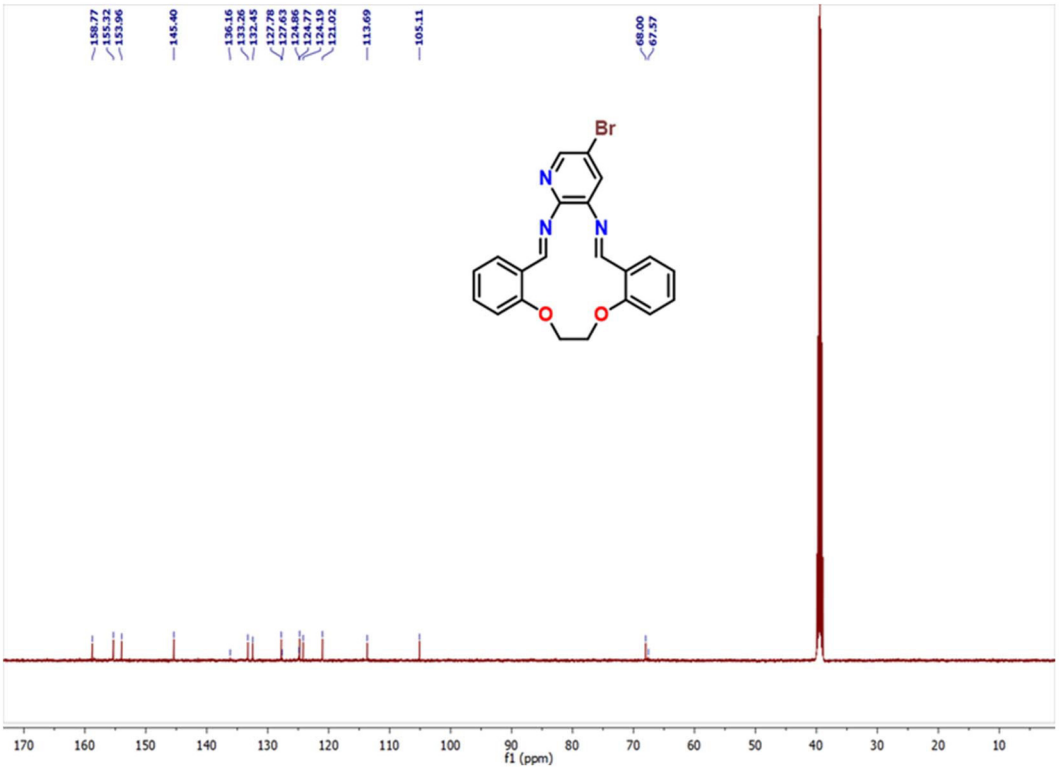

Fig. 3 ^{13}C-NMR spectrum of ligand **4**.

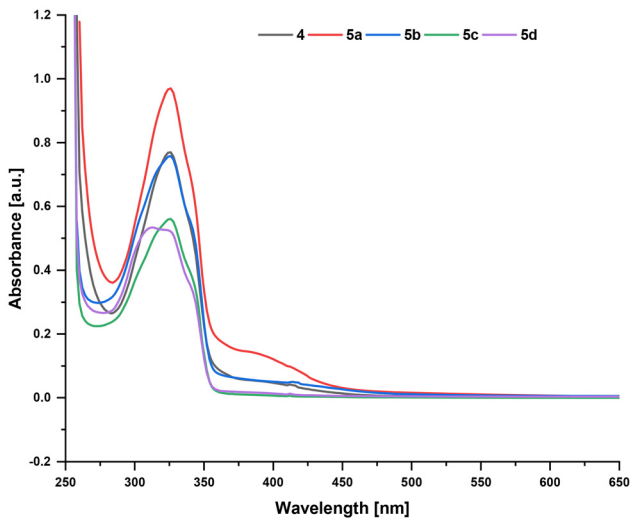

Fig. 4 UV-Vis spectra of all the newly synthesized compounds.

414 nm that is due to d–d transitions, which may correspond to the $^4T_{1g}(F) \rightarrow {}^4T_{2g}(P)$ transition. This corresponds to the octahedral geometry of the Co(II) complex (**5c**).[51] Similarly, the Cu(II) complex (**5b**) showed absorption bands at 312 nm and 326 nm, which are due to the $\pi \rightarrow \pi^*$ and $n \rightarrow \pi^*$ transitions. Other than that, three weak d–d transition bands appeared at 390, 414, and 626 nm. These are due to the Jahn Teller effect, resulting in the splitting of the ^2E_g and $^2T_{2g}$ states into lower states: $^2B_{1g}$ and $^2A_{1g}$ from ^2E_g, and $^2B_{2g}$ and ^2E_g from $^2T_{2g}$. This splitting allows for three electronic transitions from the $^2B_{1g}$ ground state ($^2B_{1g} \rightarrow {}^2A_{1g}$, $^2B_{1g} \rightarrow {}^2B_{2g}$, and $^2B_{1g} \rightarrow {}^2E_g$), whereas only one transition can be observed in an undistorted octahedral complex. These spectral features are indicative of a distorted octahedral geometry for the Cu(II) complex.[52]

The Ni(II) complex (**5d**) exhibited two prominent absorption bands and one weak absorption band at 312 nm, 326 nm and 442 nm. These transitions are likely a combination of ligand-to-metal charge transfer (LMCT) involving the π orbitals of the aromatic rings and the metal d orbitals, and d–d transitions within the Ni(II) ion. The presence of d–d transitions, particularly that indicated by the band at 442 nm, suggests an octahedral geometry for the Ni(II) complex, consistent with precedents in the literature.[42]

2.5. EPR analysis

Electron paramagnetic resonance (EPR) spectroscopy was utilized to examine the electronic environment surrounding the Cu(II) ion in complex **5b**. The EPR spectrum of the powdered complex was recorded at room temperature (300 K), as shown in Fig. 5. Analysis of the spectrum yielded $g_{\parallel} = 2.4314$ and $g_{\perp} = 2.0693$. The observed trend, $g_{\parallel} > g_{\perp} > 2.0023$, is indicative of axial symmetry around the Cu(II) ion, with the unpaired electron predominantly localized in the $d_{x^2-y^2}$ orbital.[53,54] The average *g*-value (g_{av}) was calculated to be 2.094, which deviates from the free electron *g*-value (2.0023). This deviation is attributed to the covalent character of the Cu(II)–ligand bonds, as

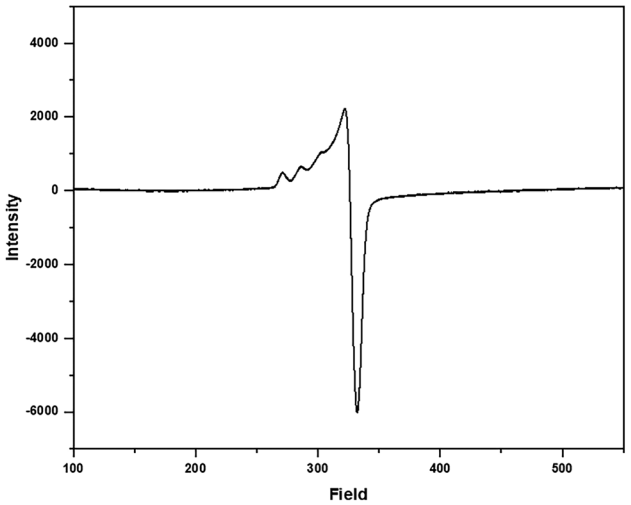

Fig. 5 EPR spectrum of the Cu(II) complex **5b**.

described by Kivelson and Neiman.[55] Consequently, the EPR spectral data strongly suggest a distorted octahedral geometry for the Cu(II) complex.

2.6. TGA analysis

The thermal stability of the synthesized complexes was investigated using thermogravimetric analysis (TGA), and the resulting decomposition profiles are presented in Fig. S13.† The plotted thermograph, which displays percentage mass loss as a function of temperature, provides valuable insights into the composition, thermal stability, and decomposition pathways of the analyzed material.[45,46] Specifically, TGA can effectively differentiate between lattice-held (crystalline) solvent or water molecules, which are located outside the primary coordination sphere of the central metal ion, and coordinated solvent or water molecules, which are directly bonded to the metal centre.[56] The TGA curves revealed multi-step decomposition processes, typically involving three to four distinct stages.

The Zn(II) complex (**5a**) exhibited exceptional thermal stability, showing no significant weight loss up to 200 °C, confirming the lack of coordinated water molecules. Decomposition commenced in three stages: (1) between 200 °C and 355 °C, a 30% mass loss attributed to nitrate ion elimination and OCH_2 bond dissociation; (2) from 356 °C to 708 °C, a 24% mass loss corresponding to salicylaldehyde moiety dissociation; and (3) complete ligand degradation by 878 °C, leaving zinc oxide and C and H residues as a 37% proportion.

The Cu(II) complex (**5b**) showed minor weight loss below 100 °C, likely due to release of residual solvent. However, the absence of weight loss between 100 °C and 200 °C confirmed the absence of coordinated water. Decomposition proceeded with nitrate ion and ether moiety dissociation from 200 °C to 364 °C, followed by partial ligand degradation by 850 °C, resulting in a total mass loss of 35.14%. The Co(II) complex (**5c**) displayed a similar decomposition pattern, initiating degradation at 238 °C. The first stage (238 °C–406 °C) resulted in a 49% mass loss, attributed to pyridine moiety dissociation. The second stage involved ether group degradation, leading to a 9.05% mass loss. Complete organic component degradation occurred by 873 °C. Similarly, the Ni(II) complex (**5d**) exhibited a two-step decomposition: (1) 200 °C–454 °C, corresponding to nitrate ion and pyridine moiety loss and (2) 455 °C–873 °C, attributed to ether moiety loss.

2.7. Molecular modelling and geometry optimization

Computational studies at the B3LYP/6-311G (d, p) and LANL2DZ level revealed that ligand **4** and complexes **5a–5d** adopt six-coordinated octahedral geometries. The optimized structures of the synthesized compounds are shown in Fig. S14.† Analysis of bond lengths confirmed the coordination of the metal atom through both the azomethine (C═N) and C–O groups: the C–N and C14–O17 bond lengths also increased on complexation from 1.43 Å to 1.47–1.49 Å and from 1.42 Å to 1.46–1.48 Å, respectively, as shown in Table S1,† indicating the phenolic oxygen coordination. The M–N31 distances in the complexes varied slightly, following the order **5c** < **5a** < **5b** < **5d**. The changes in the bond lengths of ligand and complexes follow an order that indicates the octahedral geometry. Some selected bond angles of the optimized complexes are also shown in Table S2.†

2.8. DFT studies

Electronic transitions, primarily involving HOMO excitation, are fundamental to molecular energy transfer. The HOMO–LUMO energy gap, or band gap, critically determines a molecule's stability and reactivity. A larger band gap corresponds to increased stability due to the higher energy required for electron excitation, while a smaller gap indicates greater reactivity.[57] This relationship is crucial for designing materials for applications like organic solar cells and LEDs.[58] In drug design, balancing stability (wide band gap) and reactivity (narrow band gap) is essential for efficacy and safety, ensuring resistance to degradation while facilitating targeted delivery and minimizing side effects.

The calculated HOMO–LUMO energy gaps (Fig. 6) revealed a trend of decreasing stability and increasing reactivity from the Zn(II) complex (**5a**, 3.66 eV) to the Ni(II) complex (**5d**, 3.18 eV), with the order **4** > **5a** > **5b** > **5c** > **5d**. This trend, indicative of the ease of electron excitation, was further supported by the analysis of ionization potential (P_i), electronegativity (χ), hardness (η), softness (σ), chemical potential (μ), electronic charge (ΔN) and electrophilicity index (ω), as shown in Table 1. Also, complex **5d** showed the lowest band gap, *i.e.*, 3.18 eV, which indicates the possibility of this complex exhibiting greater biological activity and electrical conductivity than other complexes.[45,59]

Chemical potential (μ) directly relates to a compound's reactivity, with higher values indicating a greater tendency for chemical interactions; thus, compounds **4** (−4.12), **5c** (−4.8), and **5d** (−4.95) are more reactive than **5a** (−5.1) and **5b** (−5.13). Further observations show that global softness (σ) values are consistently lower than global hardness (η) values for the

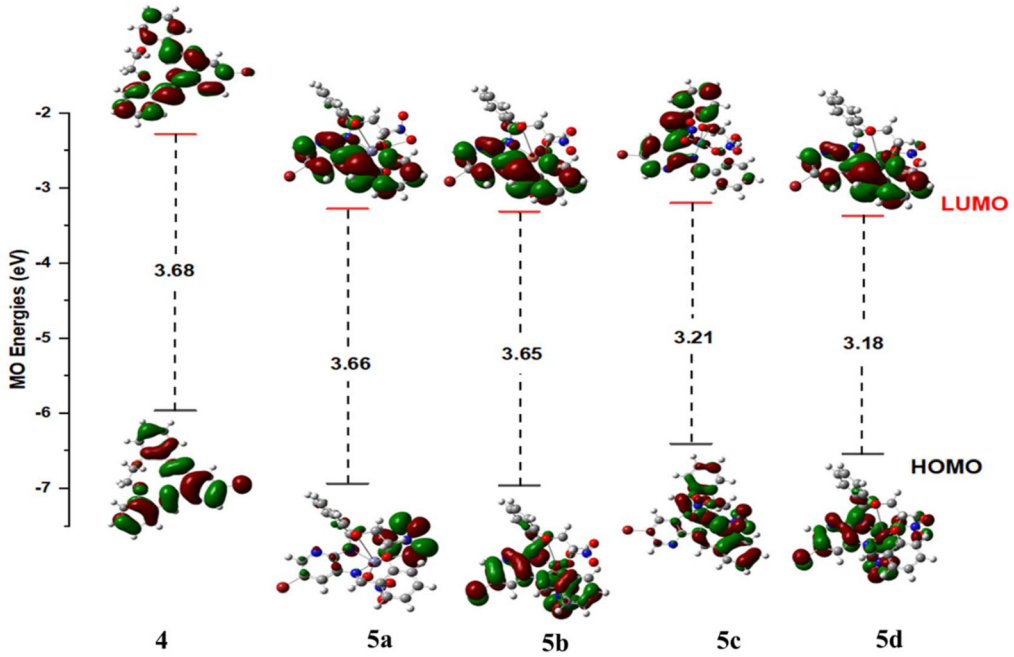

Fig. 6 HOMO–LUMO energy gap representation of all the newly synthesized compounds.

Table 1 Quantum parameters of the synthesized compounds

Quantum parameters	4	5a	5b	5c	5d
E_{HOMO} (eV)	−5.96	−6.93	−6.96	−6.40	−6.54
E_{LUMO} (eV)	−2.28	−3.27	−3.31	−3.19	−3.36
ΔE (eV)	3.68	3.66	3.65	3.21	3.18
χ (eV)	4.12	5.10	5.13	4.80	4.95
η (eV)	1.84	1.83	1.82	1.60	1.59
σ (eV)	0.54	0.55	0.55	0.62	0.63
μ (eV)	−4.12	−5.10	−5.13	−4.80	−4.95
ω (eV)	4.61	7.12	7.22	7.17	7.72
ΔN	2.24	2.78	2.81	3.0	3.11

studied ligand and complexes, which imply a general trend of high kinetic stability and low chemical reactivity. Furthermore, molecular properties such as softness (σ) and electronegativity (χ) were all higher in the complexes compared to the free ligand, suggesting enhanced electron delocalization and interaction capabilities; in particular, the electronegativity order was **5b** (5.13) > **5a** (5.10) > **5d** (4.95) > **5c** (4.80) > **4** (4.12). The high electrophilicity index (ω) values, particularly for **5d** (7.72), **5b** (7.22), and **5c** (7.17), correlate with their strong electron-accepting nature and potential as ligands for receptor binding. Notably, the Ni(II) complex (**5d**) exhibited the highest electrophilicity (7.72 eV), while the Cu(II) complex (**5b**) displayed a pronounced electronegativity (5.13 eV), suggesting potential catalytic applications. All complexes showed positive chemical potential values, indicating stability, and significant molecular softness. These findings underscore the influence of metal coordination on electronic properties and highlight the potential of these complexes for applications requiring tailored reactivity and stability.[60]

2.9. Molecular docking

In silico molecular docking simulations were performed to predict the binding energies of the synthesized complexes with respect to topoisomerase IIβ (PDB: 4G0V), a validated anticancer target. This approach was aimed at elucidating potential anticancer mechanisms by analyzing the interactions between the complexes and the protein's active site. Fig. 7 depicts the lowest energy docking pose for ligand **4**, while Table 2 summarizes the key amino acid residues involved in H-bonding and other interactions, comparing these with the standard drug doxorubicin (DOX). Additional 3D and 2D docking visualizations are provided in Fig. S15–S18.†

Molecular docking analysis revealed significant interactions between the synthesized ligand, its metal complexes and topoisomerase IIβ, involving both hydrogen bonding and other interactions. Notably, the ligand itself exhibited the strongest binding affinity (−10.3 kcal mol^{-1}), characterized by π–alkyl interaction with ALA817 and hydrogen-bond interactions with GLN805, SER480, ASP815, DG10, and SER483 residues critical for catalysis and binding. These interactions appear to stabilize the ligand within the active site, contributing to strong binding affinity. The metal complexes also exhibited varying degrees of binding affinity, as shown in Table 2. The order of calculated binding affinities for the compounds with topoisomerase IIβ followed the trend **4** > **5b** > **5c** > **5a** > **5d**.

An examination of the binding modes and hydrogen bonding interactions between the receptor and ligands, derived from AutoDock Vina data, is presented in Fig. 7, S15–18† and Table S3,† revealing distinct interaction patterns. Ligand **4** engaged in five moderate to weak H-bonds with the receptor ranging in length from 2.89 to 4.01 Å, involving

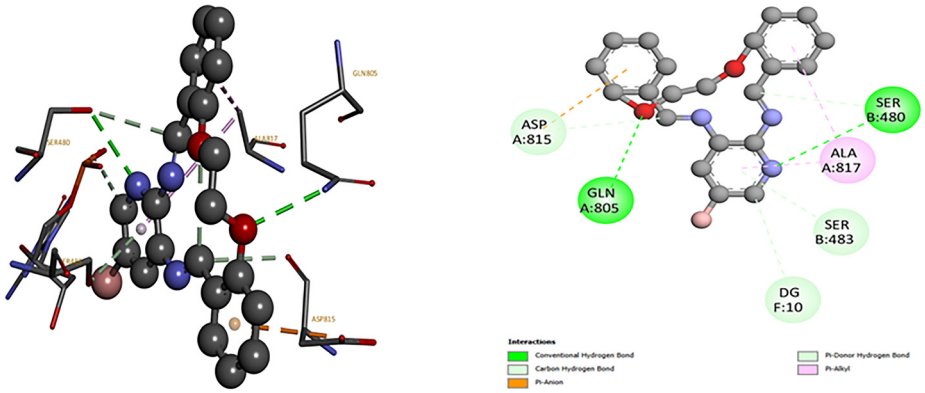

Fig. 7 Interactions of ligand **4** with the active site of topoisomerase IIβ protein docked using AutoDock Vina.

Table 2 Calculated docking parameters of the compounds with topoisomerase IIβ enzyme (PDB: 4G0V) from AutoDock Vina

Sr. No.	Compound	Interacting residue	B.E. (kcal mol^{-1})	IC_{50} (μM)
1.	**4**	GLN805, SER480, ASP815, DG10, SER483, and ALA817	−10.3	0.09
2.	**5a**	SER818, ALA817, PRO819, VAL785, LYS814, MET782, DG10, and DC11	−9.8	0.12
3.	**5b**	DA12, SER818, DC11, ARG820, PRO819, and MET782	−10.1	0.1
4.	**5c**	ALA816, DC11, MET782, VAL785, PRO819, and DG10	−10.0	0.1
5.	**5d**	DA12, SER818, MET782, PRO819, ARG820, and DC11	−9.45	0.13
6.	DOX	GLN778, DC8, DT9, DA12, DG13, and DA12	−10.6	0.02

Table 3 Calculated docking parameters of the compounds with the topoisomerase IIβ enzyme (PDB: 4G0V) from GOLD software

Sr. No.	Compound	Interacting residue	B.E. (kcal mol^{-1})	IC_{50} (μM)
1.	**4**	DG1362, DA1361, DT1338, DC1337, ARG52, and GLU71	75.27	0.09
2.	**5a**	ARG52, GLU71, DG1339, DA1361, DC1340, PRO4, and LYS5	49.48	0.12
3.	**5b**	DG1339, DC1340, GLU71, ARG52, LYS5, PRO4, and PRO50	60.9	0.1
4.	**5c**	DA1361, DG1362, GLU71, and ARG52	53.6	0.1
5.	**5d**	DG1339, ARG52, DC1340, PRO4, and DA1361	48.58	0.13
6.	DOX	GLN778, DC8, DT9, DA12, DG13, and DA12	66.32	0.02

O···H–N_{GLN805}, three C–H···$O_{ASP815,\ SER480,\ DG10}$, and C···H–$O_{SER483}$ bonds. Complexes **5a**, **5b** and **5d** each displayed two H-bond interactions with the receptor having 2.83–3.79 Å (O–H···O_{SER818} and O···H–C_{ALA817}), 3.13–3.59 Å (O···H–N_{DA12} and C–H···O_{ALA816}), and 3.08–3.80 Å (O···H–N_{DA12} and C–H···O_{SER818}) bond distances, respectively. In contrast, complex **5c** formed only one H-bond with the receptor, a C–H···O_{SER818} interaction with a bond distance of 3.79 Å.

To gain deeper insight into the binding interactions, docking simulations were conducted employing the GOLD scoring function. This sophisticated method evaluated the binding affinity between the synthesized compounds and topoisomerase IIβ (PDB: 4G0V), a well-established target in cancer therapeutics. The outcomes of this analysis are summarized in Table 3. The lowest-energy docked conformation of ligand **4** within the target protein's active site, as determined by the GOLD score, is shown in Fig. 8. Notably, the Schiff-base ligand **4** exhibited the highest GOLD score (75.27 kcal mol^{-1}) among the series, indicating a strong binding affinity even more than that of the standard drug. Visual inspection of the docked pose revealed favorable interactions with residues ARG52, GLU71, DC1337, DT1338, DA1361, and DG1362, as shown in Fig. 8. Importantly, the rank order of the predicted binding affinities based on the GOLD scores (**4** > **5b** > **5c** > **5a** > **5d**) aligns with the binding affinity trends previously observed using AutoDock Vina, providing further confidence in the docking results.

Analysis of GOLD docking data revealed varying H-bonding interactions between the receptor and the ligand or its complexes, as shown in Table S3† and Fig. 8, S19–S22.† Notably, ligand **4** exhibited no H-bond interactions with the receptor. In contrast, complex **5a** formed five moderate to weak H-bonds with distances ranging from 2.01 to 4.28 Å, involving O···H–N_{DG1339}, C–H···O_{GLU71}, two O···H–$C_{ARG52,\ DC1340}$, and N···H–C_{DA1361} bonds. Both complexes **5b** and **5c** had three H-bond interactions with bond distances of 2.11–2.30 Å (C–H···O_{GLU71}, O···H–C_{DC1340}, and O···H–N_{DG1339}) and 2.24–3.00 Å (C–H···O_{GLU71}, O···H–C_{DG1362}, and C–H···O_{DA1361}). Finally, complex **5d** engaged in four H-bond interactions with the receptor, with bond distances of 1.69–2.91 Å, involving C–H···O_{DA1361}, 2O···H–$N_{ARG52,\ DG1339}$, and O···H–C_{DC1340} bonds.

2.10. Cytotoxicity

Based on the encouraging *in silico* docking results, which indicated favorable interactions between the crucial anticancer

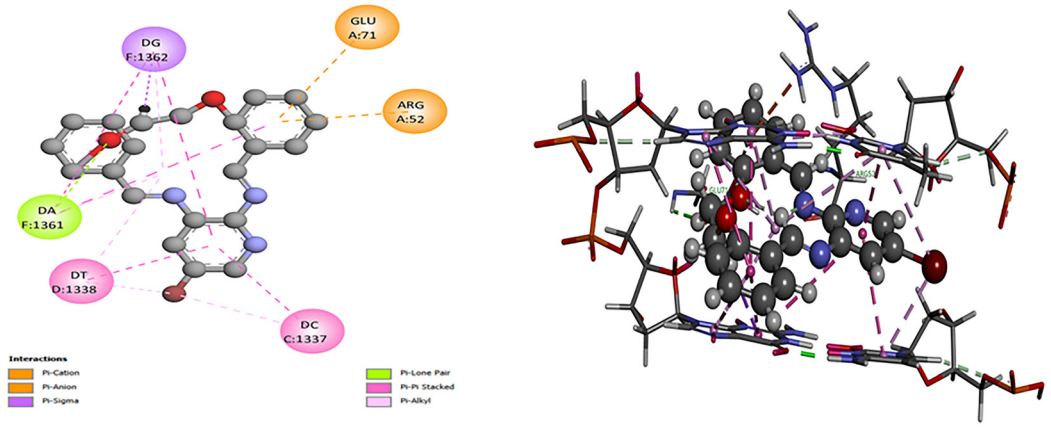

Fig. 8 Interactions of ligand **4** with the active site of topoisomerase IIβ protein docked using GOLD.

target topoisomerase IIβ and the synthesized compounds, we proceeded to evaluate the *in vitro* anticancer activity of these compounds against the HepG2 cancer cell line. Utilizing the MTT assay, we assessed the cytotoxicity of the compounds at various concentrations. Interestingly, the projected binding affinities obtained from the docking studies precisely corresponded to the trend in the experimentally measured IC_{50} values.

The relationship between the different concentrations and the resulting % inhibition of cell growth is shown graphically in Fig. 9. From this dose–response data, the half-maximal inhibitory concentration (IC_{50}) for each compound was determined and is presented in Table S4.† Furthermore, morphological alterations in HepG2 cells following 24 h of treatment with their respective IC_{50} concentrations were documented through microscopy and are shown in Fig. 10 and Fig. S23,† allowing for a direct comparison with untreated control cells. The calculated IC_{50} values for the synthesized compounds were 0.09 μM (ligand **4**), 0.12 μM (**5a**), 0.1 μM (**5b** and **5c**), and 0.13 μM (**5d**). Comparative analysis revealed that the Schiff-base ligand **4** exhibited the most potent cytotoxic effect, displaying an IC_{50} value of 0.09 μM, which is remarkably close to that of the standard anticancer drug doxorubicin (IC_{50} = 0.02 μM).[61] According to these results, ligand **4** demonstrates a great deal of promise as a potent anticancer drug against the HepG2 liver cancer cell line and needs more research.

Also, the consistent correlation between the computational predictions, *i.e. in silico* docking results and the *in vitro* findings, provides strong evidence supporting the potential of these synthesized compounds as effective anticancer agents targeting topoisomerase IIβ in liver cancer cells. The anticancer results of the synthesized ligand **4** and complexes **5a–5d** are in accordance with the literature reports on salophen-type Schiff-base moieties.[62–66] Also, our compounds showed better IC_{50} values in comparison with the reported ones.

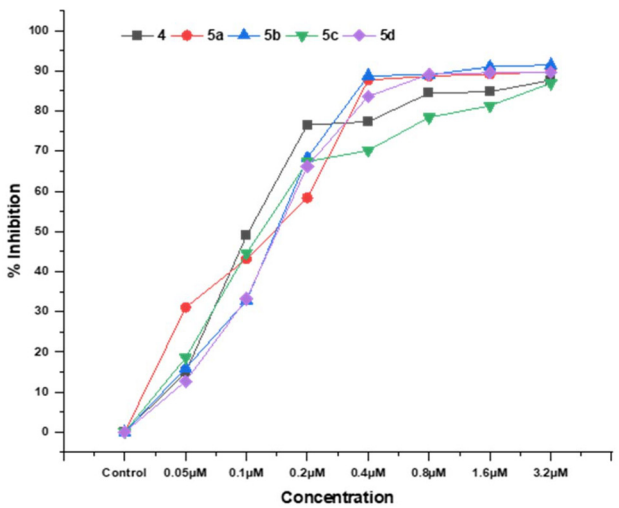

Fig. 9 Inhibition % *vs.* concentration representation of compounds **4** and **5a–5d**.

2.11. Hemolysis

Drug-induced hemolysis, characterized by the destruction of red blood cells, represents a recognized adverse effect associated with certain chemotherapeutic agents. This complication often stems from the interaction of drugs with the erythrocyte membrane, particularly the delicate phospholipid bilayer. Disruption of this critical structure can compromise the membrane's integrity, ultimately leading to cell lysis and hemolytic anemia.[67] Recognizing the potential for hemolytic complications, especially with metal-based drugs, and then evaluating the hemolytic potential of our newly synthesized compounds are of paramount importance. This assessment provides crucial insight into their safety profile and informs their suitability for further preclinical and clinical development.

To evaluate the potential for systemic toxicity, we conducted hemolysis analysis of the synthesized compounds against human red blood cells (hRBCs). The results indicated a favorable safety profile, as all compounds demonstrated minimal hemolytic activity. Even at the highest tested concentration of 1.6 μM, the maximum lysis of hRBCs observed was only 15%

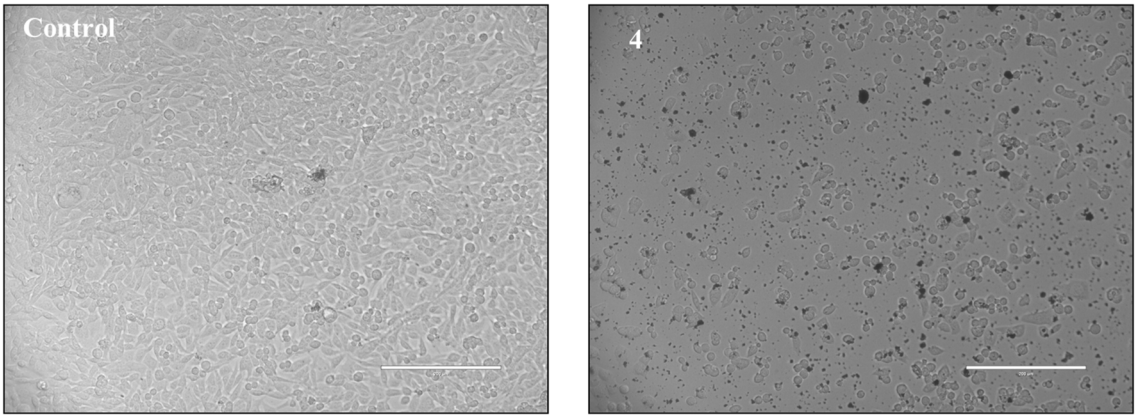

Fig. 10 Morphological alterations in the cells after 24 h of treatment with ligand **4**.

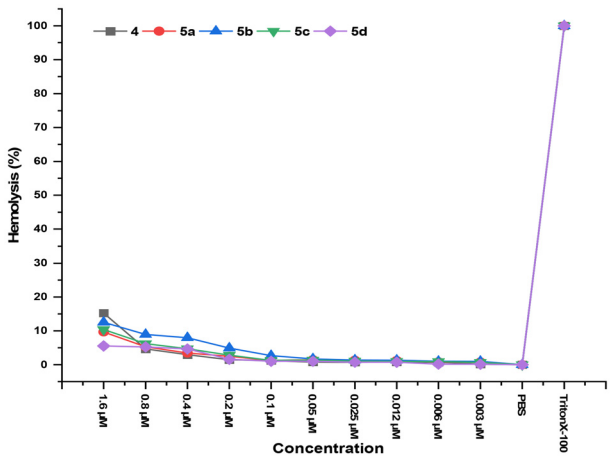

Fig. 11 Hemolysis activity of the synthesized compounds.

(shown in Fig. 11). Importantly, at concentrations corresponding to their respective IC_{50} values determined in the anticancer assays, all compounds exhibited less than 2% lysis of hRBCs, which indicated their non-toxic nature.[68]

3. Conclusions

In summary, we have synthesized a salophen-type macrocyclic Schiff-base ligand and its metal complexes and evaluated their structural data by using various spectral techniques. The spectral analysis concluded that all the complexes exist as structures with octahedral geometry. The ESR spectrum of the Cu (II) complex revealed that it has a distorted octahedral geometry. Computational investigations employing DFT methods elucidated the geometrical structures of these compounds. Furthermore, *in silico* docking simulations utilizing AutoDock Vina and GOLD scoring functions predicted favorable binding interactions between the synthesized compounds and topoisomerase IIβ, a critical enzyme target in cancer therapy. Notably, ligand **4** exhibited the most promising binding affinity (−10.3 kcal mol^{-1}), attributed to specific hydrogen-bonding interactions with key amino acid residues within the topoisomerase IIβ active site. This computational prediction was strongly corroborated by *in vitro* cytotoxicity assays using the MTT assay, whereupon ligand **4** demonstrated the most potent inhibitory activity against cancer cells, displaying an IC_{50} value of 0.09 μM. This significant alignment between the *in silico* and the *in vitro* studies underscores the potential of these compounds to exert their anticancer effects through topoisomerase IIβ inhibition. Overall, our findings highlight the synthesized compounds, particularly ligand **4**, as promising lead compounds for the development of novel anticancer drugs targeting topoisomerase IIβ. Further comprehensive investigations are warranted to elucidate their detailed mechanism of action, pharmacodynamic properties, *etc*.

Author contributions

Monika Yadav: conceptualization, investigation, writing – original draft, writing – review and editing, methodology, software, data curation, formal analysis, and resources. Deepak Yadav: methodology, conceptualization, writing – review and editing, software, data curation, and investigation. Dharam Pal Singh: conceptualization, validation, visualization, writing – review and editing, project administration, and supervision. Jitander Kumar Kapoor: conceptualization, funding acquisition, methodology, writing – review and editing, project administration, supervision, resources, and data curation.

Data availability

The data supporting this article have been included as a part of the ESI.†

Conflicts of interest

The authors declare no conflicts of interest.

Acknowledgements

The authors are thankful to NIT Kurukshetra for providing laboratory facilities and financial support. The authors are grateful to the Department of Experimental Medicine and Biotechnology, PGIMER Chandigarh for facilitating the biological studies.

References

1 U. Anand, A. Dey, A. K. S. Chandel, R. Sanyal, A. Mishra, D. K. Pandey, V. De Falco, A. Upadhyay, R. Kandimalla, A. Chaudhary, J. K. Dhanjal, S. Dewanjee, J. Vallamkondu and J. M. Pérez De La Lastra, *Genes Dis.*, 2023, **10**, 1367–1401.
2 D. E. Thurston and I. Pysz, *Chemistry and Pharmacology of Anticancer Drugs*, CRC Press, Boca Raton, 2nd edn, 2021.
3 S. Dallavalle, V. Dobričić, L. Lazzarato, E. Gazzano, M. Machuqueiro, I. Pajeva, I. Tsakovska, N. Zidar and R. Fruttero, *Drug Resistance Updates*, 2020, **50**, 100682.
4 M. Kciuk, A. Gielecińska, S. Mujwar, D. Kołat, Ż Kałuzińska-Kołat, I. Celik and R. Kontek, *Cells*, 2023, **12**, 659.
5 W. Chen, J. Qui and Y. Shen, *Drug Discoveries Ther.*, 2012, **6**, 230–237.
6 Y. Pommier, *ACS Chem. Biol.*, 2013, **8**, 82–95.
7 K. Bukowski, M. Kciuk and R. Kontek, *Int. J. Mol. Sci.*, 2020, **21**, 3233.
8 J. L. Nitiss, *Nat. Rev. Cancer*, 2009, **9**, 338–350.
9 P. Rajakkani, A. Alagarraj and S. A. Gurusamy Thangavelu, *Inorg. Chem. Commun.*, 2021, **134**, 108989.
10 B. N. Ma, D. Baecker, H. Descher, P. Brandstaetter, M. Hermann, B. Kircher and R. Gust, *Arch. Pharm.*, 2023, **356**, 2200655.
11 J. Devi, S. Devi and A. Kumar, *Med. Chem. Commun.*, 2016, **7**, 932–947.
12 L. A. Alfonso-Herrera, D. Hernández-Romero, J. A. Cruz-Navarro, Á. Ramos-Ligonio, A. López-Monteon, J. M. Rivera-Villanueva, D. Morales-Morales and R. Colorado-Peralta, *Coord. Chem. Rev.*, 2024, **505**, 215698.
13 I. P. Ejidike, A. Direm, C. Parlak, A. A. Adeniyi, M. Azam, A. Ata, M. O. Eze, J. W. Hollett and H. S. Clayton, *Chem. Phys. Impact*, 2024, **8**, 100549.
14 R. O. Awolope, I. P. Ejidike and H. S. Clayton, *J. Appl. Pharm. Sci.*, 2023, **13**, 132–140.
15 N. H. Boukoucha, Z. Messasma, D. Aggoun, Y. Ouennoughi, C. Bensouici, M. Fernández-García, D. Lopez, M. Guelfi, F. Marchetti, G. Bresciani and Z. Chorfi, *J. Mol. Struct.*, 2025, **1319**, 139505.
16 W. A. Wani, A. Hussain, S. Amir, M. F. Alajmi, A. H. Malik, A. Khursheed and W. A. Khanday, in *ACS Symposium Series*, American Chemical Society, Washington, DC, 2025, vol. 1492, pp. 1–12.
17 D. Fan, Y. Cao, M. Cao, Y. Wang, Y. Cao and T. Gong, *Signal Transduction Targeted Ther.*, 2023, **8**, 293.
18 L. Canali and D. C. Sherrington, *Chem. Soc. Rev.*, 1999, **28**, 85–93.
19 E. M. McGarrigle and D. G. Gilheany, *Chem. Rev.*, 2005, **105**, 1563–1602.
20 M. T. Kaczmarek, M. Zabiszak, M. Nowak and R. Jastrzab, *Coord. Chem. Rev.*, 2018, **370**, 42–54.
21 S. T. Tsantis, D. I. Tzimopoulos, M. Holynska and S. P. Perlepes, *Int. J. Mol. Sci.*, 2020, **21**, 555.
22 Y.-S. Wei, M. Zhang, R. Zou and Q. Xu, *Chem. Rev.*, 2020, **120**, 12089–12174.
23 R. Mazzoni, F. Roncaglia and L. Rigamonti, *Crystals*, 2021, **11**, 483.
24 Y. Lin, H. Betts, S. Keller, K. Cariou and G. Gasser, *Chem. Soc. Rev.*, 2021, **50**, 10346–10402.
25 M. Karmakar, S. Roy and S. Chattopadhyay, *Polyhedron*, 2022, **215**, 115652.
26 A. Goudarzi, M. Saeidifar, K. Aghapoor, F. Mohsenzadeh, D. Fenske, O. Fuhr and M. Ghassemzadeh, *J. Mol. Struct.*, 2023, **1272**, 134224.
27 F. Deng, X. Li, F. Ding, B. Niu and J. Li, *J. Phys. Chem. C*, 2018, **122**, 5325–5333.
28 A. Erxleben, *Inorg. Chim. Acta*, 2018, **472**, 40–57.
29 M. Aligholivand, Z. Shaghaghi, R. Bikas and A. Kozakiewicz, *RSC Adv.*, 2019, **9**, 40424–40436.
30 S. Shaw and J. D. White, *Chem. Rev.*, 2019, **119**, 9381–9426.
31 N. Aggarwal and S. Maji, *Rev. Inorg. Chem.*, 2022, **42**, 363–383.
32 M. Pervaiz, A. Sadiq, S. Sadiq, Z. Saeed, M. Imran, U. Younas, S. Majid Bukhari, R. Rashad Mahmood Khan, A. Rashid and A. Adnan, *Inorg. Chem. Commun.*, 2022, **137**, 109206.
33 I. Yoon, M. Goto, T. Shimizu, S. S. Lee and M. Asakawa, *Dalton Trans.*, 2004, 1513–1515.
34 J. Gao, J. H. Reibenspies, R. A. Zingaro, F. R. Woolley, A. E. Martell and A. Clearfield, *Inorg. Chem.*, 2005, **44**, 232–241.
35 S. Akine, F. Utsuno, S. Piao, H. Orita, S. Tsuzuki and T. Nabeshima, *Inorg. Chem.*, 2016, **55**, 810–821.
36 S. Akine, S. Piao, M. Miyashita and T. Nabeshima, *Tetrahedron Lett.*, 2013, **54**, 6541–6544.
37 D. Villaman, A. Vega, L. Santa Maria De La Parra, I. E. León, P. Levín and P. M. Toro, *Dalton Trans.*, 2023, **52**, 10855–10868.
38 S. Y. Ebrahimipour, M. Mohamadi, M. Torkzadeh Mahani, J. Simpson, J. T. Mague and I. Sheikhshoaei, *Eur. J. Med. Chem.*, 2017, **140**, 172–186.
39 J. Vančo, Z. Šindelář, Z. Dvořák and Z. Trávníček, *J. Inorg. Biochem.*, 2015, **142**, 92–100.
40 Z. K. Yilmaz, Ö. Özdemir, B. Aslim, Z. Suludere and E. Şahin, *J. Biomol. Struct. Dyn.*, 2023, **41**, 2804–2822.
41 C. Gökçe Topkaya, T. Göktürk, T. Hökelek, E. Sakalli Çetin, S. Kincal and R. Güp, *J. Mol. Struct.*, 2022, **1266**, 133453.
42 M. Yadav, D. Yadav, D. P. Singh and J. K. Kapoor, *Appl. Organomet. Chem.*, 2025, **39**, e7885.

43 M. Yadav, D. Yadav, S. Kansal, A. Angrup, N. Taneja, D. P. Singh and J. K. Kapoor, *J. Mol. Struct.*, 2024, **1317**, 139078.
44 S. Anila Raj, V. G. Vidya, V. Preethi and V. G. Viju Kumar, *Results Chem.*, 2022, **4**, 100665.
45 I. P. Ejidike, A. Direm, C. Parlak, S. A. Olaleru, C. O. Adetunji, F. M. Mtunzi, A. Ata, M. O. Eze, H. S. Clayton, P. A. Ajibade and J. W. Hollett, *Results Chem.*, 2025, **15**, 102219.
46 I. P. Ejidike, M. O. Bamigboye and H. S. Clayton, *Spectrosc. Lett.*, 2021, **54**, 212–230.
47 X.-H. Lu, Q.-H. Xia, H.-J. Zhan, H.-X. Yuan, C.-P. Ye, K.-X. Su and G. Xu, *J. Mol. Catal. A: Chem.*, 2006, **250**, 62–69.
48 S. Amer, N. El-Wakiel and H. El-Ghamry, *J. Mol. Struct.*, 2013, **1049**, 326–335.
49 Z. Fang, C. Cao and G. Chen, *J. Phys. Org. Chem.*, 2012, **25**, 1343–1350.
50 S. Ilhan, H. Temel, I. Yilmaz and M. Sekerci, *J. Organomet. Chem.*, 2007, **692**, 3855–3865.
51 N. Jyothi, N. Ganji, S. Daravath and Shivaraj, *J. Mol. Struct.*, 2020, **1207**, 127799.
52 M. J. Gajewska, W.-M. Ching, Y.-S. Wen and C.-H. Hung, *Dalton Trans.*, 2014, **43**, 14726–14736.
53 R. N. Patel, Y. Singh, Y. P. Singh and R. J. Butcher, *J. Coord. Chem.*, 2016, **69**, 2377–2390.
54 M. C. Jain, A. K. Srivastava and P. C. Jain, *Inorg. Chim. Acta*, 1977, **23**, 199–203.
55 D. Kivelson and R. Neiman, *J. Chem. Phys.*, 1961, **35**, 149–155.
56 M. Swathi, D. Ayodhya and Shivaraj, *Results Chem.*, 2024, **7**, 101231.
57 B. Kumar, J. Devi and A. Manuja, *Res. Chem. Intermed.*, 2023, **49**, 2455–2493.
58 T. Xu and L. Yu, *Mater. Today*, 2014, **17**, 11–15.
59 S. Daoui, C. Parlak, Ş. Direkel, P. Ramasami, H. A. Abuelizz, A. Oulmidi, N. Benchat and K. Karrouchi, *ChemistrySelect*, 2024, **9**, e202402996.
60 M. M. Khalaf, H. M. Abd El-Lateef, A. A. Taha and A. Abdou, *Appl. Organomet. Chem.*, 2025, **39**, e70027.
61 L. J. Lalitha, T. J. Sales, P. P. Clarance, P. Agastian, Y.-O. Kim, A. H. Mahmoud, S. E. Mohamed, J. C. Tack, S. W. Na and H.-J. Kim, *J. King Saud Univ., Sci.*, 2020, **32**, 1246–1253.
62 P. Wu, D. Ma, C. Leung, S. Yan, N. Zhu, R. Abagyan and C. Che, *Chem. – Eur. J.*, 2009, **15**, 13008–13021.
63 S. Banerjee, M. S. Capper, G. J. Clarkson, H. Huang and P. J. Sadler, *Polyhedron*, 2019, **172**, 157–166.
64 M. Gillard, J. Weynand, H. Bonnet, F. Loiseau, A. Decottignies, J. Dejeu, E. Defrancq and B. Elias, *Chem. – Eur. J.*, 2020, **26**, 13849–13860.
65 A. Ali, M. Kamra, S. Roy, K. Muniyappa and S. Bhattacharya, *Bioconjugate Chem.*, 2017, **28**, 341–352.
66 Y. Peng, H. Zhong, Z.-F. Chen, Y.-C. Liu, G.-H. Zhang, Q.-P. Qin and H. Liang, *Chem. Pharm. Bull.*, 2014, **62**, 221–228.
67 E. S. Aazam and M. Zaki, *ChemistrySelect*, 2020, **5**, 610–618.
68 M. S. Laranjeira, A. Moço, J. Ferreira, S. Coimbra, E. Costa, A. Santos-Silva, P. J. Ferreira and F. J. Monteiro, *Colloids Surf., B*, 2016, **146**, 363–374.